CHAPTER IV
RESULTS AND DISCUSSION

4.1 Catalyst Characterization

4.1.1 Elemental Analysis and BET Surface Area Measurements

The chemical compositions and BET surface areas of the support and catalyst synthesized are reported in Table 4.1. The compositions of the support was met a desired Ce/Zr molar ratio of 3:1 and the nickel (Ni) loading was determined to be ca. 15 wt%. Since small amounts of ZrO_2 were not incorporated in the CeO_2 lattices to form a solid solution as indicated by XRD results (Section 4.1.2), the catalyst prepared in this research was designated as 15%Ni/Ce75Zr25Ox. Moreover, BET surface area was found to decrease after being impregnated with Ni from 95.73 to 74.08 m^2/g. The decrease in surface area was resulted from pore blocking by Ni loading.

Table 4.1 The chemical compositions and BET surface areas of the support and catalyst synthesized

Catalyst	Composition[a] (wt%)				Ce/Zr ratio	BET surface area (m^2/g)
	Ce	Zr	Ni	O		
Ce75Zr25Ox	68.94	14.53	-	16.52	3.09:1	95.73
15%Ni/Ce75Zr25Ox	60.87	13.21	15.14	10.77	3.00:1	74.08

[a] XRF technique

4.1.2 X-ray Diffraction (XRD)

The XRD patterns of Ce75Zr25Ox support and 15%Ni/Ce75Zr25Ox catalyst are shown in Figure 4.1. The Ce75Zr25Ox support exhibits major peaks at 28.60, 33.14, 47.42, and 56.42° (2θ) corresponding to the plane indices of (1,1,1), (2,0,0), (2,2,0), and (3,1,1), respectively, indicating a cubic fluorite structure of CeO_2 as dominant. Besides, some extra peaks of tetragonal phase of ZrO_2 were observed at 30.11, 50.23, and 59.48° (2θ) indicating some of ZrO_2 were not incorporated in the

CeO_2 lattice to form a solid solution. In the case of 15wt% Ni loading, the XRD patterns show a typical cubic fluorite structure of ceria with the presence of NiO phase at 37.33, 43.34, 63.01, and 75.50° (2θ) corresponding to the plane indices of (1,1,1), (2,0,0), (2,2,0), and (3,1,1), respectively. These results are in agreement with those reported by previous works (Phongprueksathat, 2013; Traitangwong, 2014). Moreover, the crystallite size of each plane was estimated using the Scherrer equation as shown in Table 4.2.

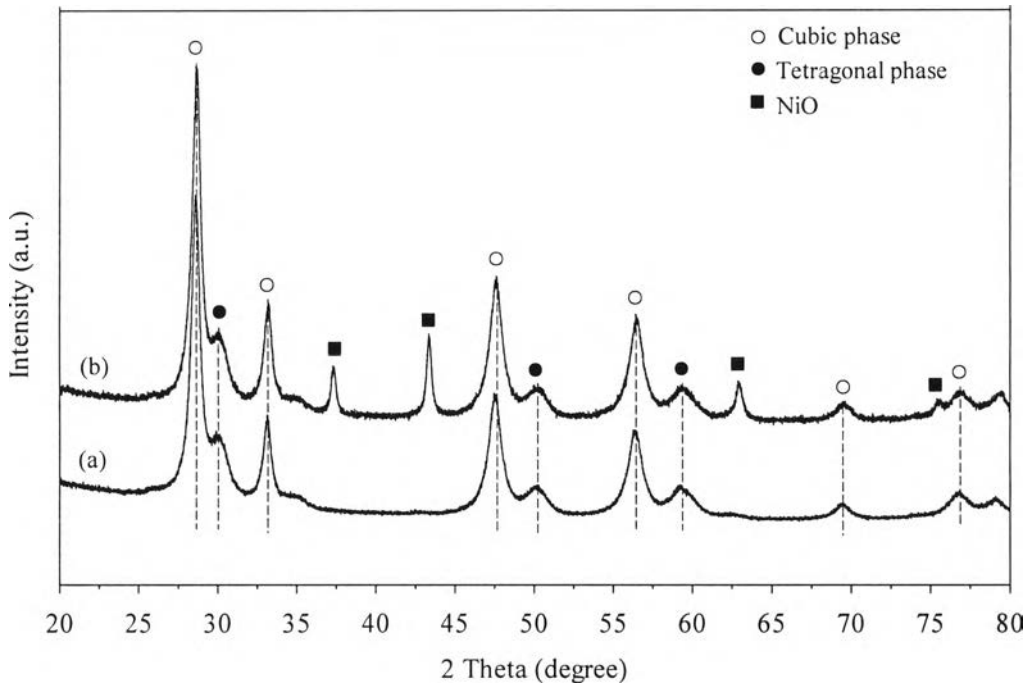

Figure 4.1 XRD patterns of (a) Ce75Zr25Ox and (b) 15%Ni/Ce75Zr25Ox.

Table 4.2 Crystallite sizes of NiO on various planes obtained from XRD analysis

Plane	**(1,1,1)**	**(2,0,0)**	**(2,2,0)**	**(3,1,1)**
Crystallite size[a] (nm)	24.21	25.81	23.94	11.27

[a] Estimated using the Scherrer equation

4.1.3 Temperature Programmed Reduction of Hydrogen (H_2-TPR)

The H_2-TPR profiles of the materials are depicted in Figure 4.2. The Ce75Zr25Ox support exhibits reduction peaks at around 410 °C and 800 °C indicative of a surface reduction and bulk reduction of CeO_2, respectively. For 15%Ni/Ce75Zr25Ox catalyst, a low temperature peak (~270 °C) was attributed to the reduction of the free NiO particles and a high temperature peak (~370 °C) was attributed to the reduction of complex NiO species in intimate contact with the support while another peak at ca. 800 °C was related to the bulk reduction of CeO_2 from Ce^{4+} to Ce^{3+} similar to that reported by Thaicharoensutcharittham *et al.* (2011).

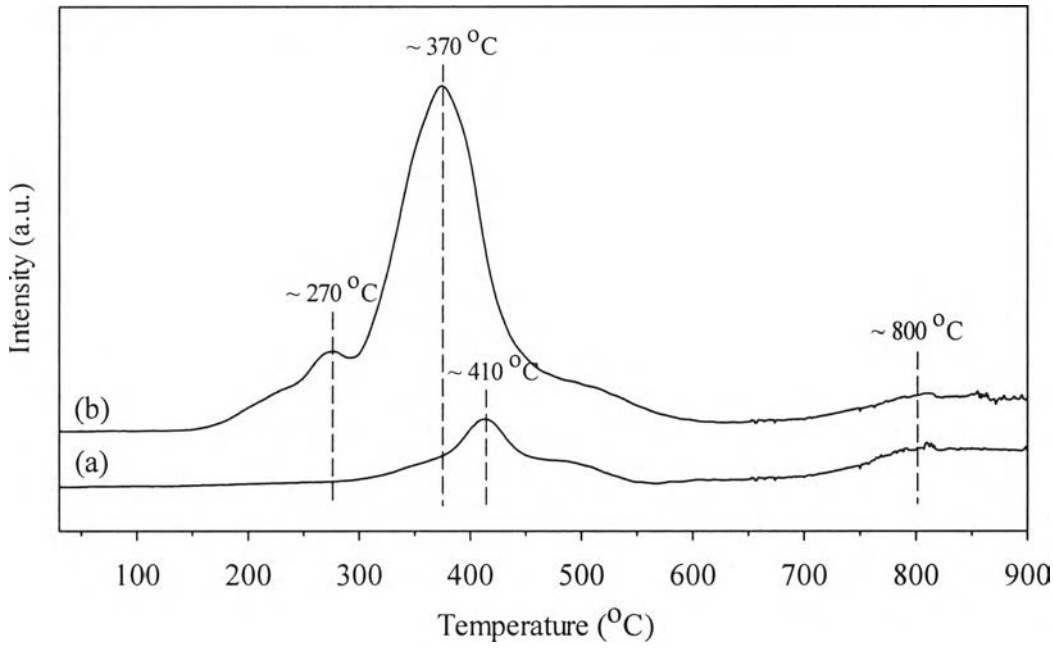

Figure 4.2 H_2-TPR profiles with heating rate of 10 °C/min, a reducing gas containing 5 % H_2 in N_2 with a flow rate of 20 ml/min, patterns of (a) Ce75Zr25Ox and (b) 15%Ni/Ce75Zr25Ox.

4.1.4 Scanning Electron Microscopy (SEM)

The morphologies of Ce75Zr25Ox support and 15%Ni/Ce75Zr25Ox catalyst are presented in Figure 4.3. All of which illustrate the aggregation of the primary long thin needle shaped particles similar to that described by Thammachart *et al.* (2001). In the presence of Ni metal, the fine particles of NiO can

be observed as the attached on the surface of the long thin needles of the Ce75Zr25Ox support.

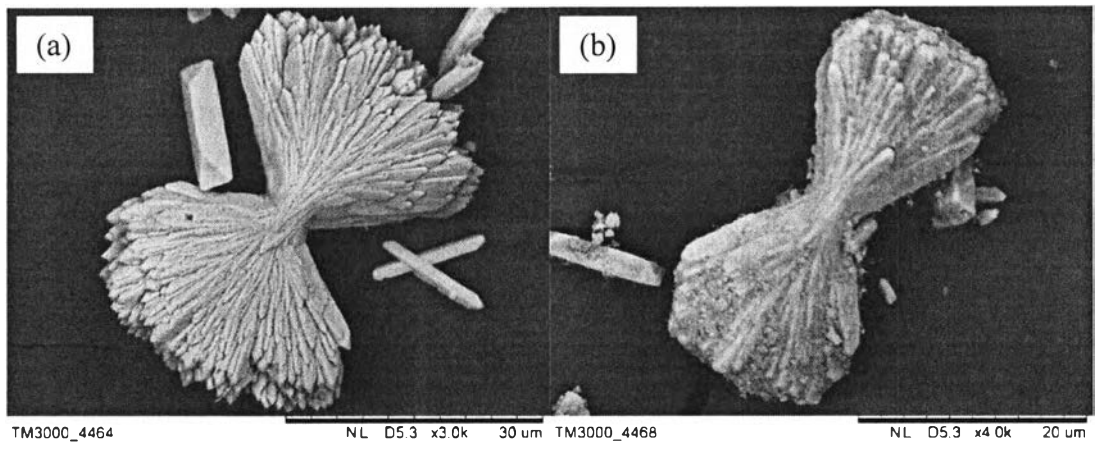

Figure 4.3 SEM images of (a) Ce75Zr25Ox and (b) 15%Ni/Ce75Zr25Ox.

4.2 Catalytic Activity Tests

Prior to testing the 15%Ni/Ce75Zr25Ox catalyst, the steam reforming (SR), partial oxidation (POX), and autothermal steam reforming (ATR) of acetic acid (CH_3COOH) were individually performed over Ce75Zr25Ox support and quartz wool under those conditions mentioned in the experimental section. The results showed that the Ce75Zr25Ox support alone had moderate C-C bond breakage conversion and converted acetic acid into H_2 and CO_2 with small amounts of CO, CH_4, and acetone (CH_3COCH_3) in SR and ATR processes while POX exhibited less H_2 production of ca. 20 % compared to those two processes. In addition, at low conversion, traces of all products were detected in all processes over quartz wool, this implies that the homogeneous reactions could be negligible. The experimental data from blank tests (the activity of Ce75Zr25Ox support and quartz wool) are summarized in Appendix E. Then, the conversions, gaseous product yields, and selectivities were investigated over the 15%Ni/Ce75Zr25Ox catalyst under different conditions, including SR, POX, and ATR of acetic acid. The reactions involved are presented in Table 4.3.

Table 4.3 The reactions involved in SR, POX, and ATR of acetic acid

Reaction	Equation	$\Delta H°_{298}$ (kJ/mol)
• Steam reforming of acetic acid		
$CH_3COOH + 2H_2O \rightarrow 4H_2 + 2CO_2$	(4.1)	131.4
• Autothermal steam reforming of acetic acid		
$CH_3COOH + 0.35O_2 + 1.3H_2O \rightarrow 3.3H_2 + 2CO_2$	(4.2)	0
• Partial oxidation of acetic acid		
$CH_3COOH + 0.5O_2 \rightarrow 2CO + H_2 + H_2O$	(4.3)	-23.0
• Oxidation of acetic acid		
$CH_3COOH + O_2 \rightarrow 2CO + 2H_2O$	(4.4)	-308.8
$CH_3COOH + 2O_2 \rightarrow 2CO_2 + 2H_2O$	(4.5)	-874.7
• Ketonization reaction		
$2CH_3COOH \rightarrow CH_3COCH_3 + CO_2 + H_2O$	(4.6)	16.7
• Decomposition of acetic acid		
$CH_3COOH \rightarrow 2CO + 2H_2$	(4.7)	213.7
• Decarboxylation of acetic acid		
$CH_3COOH \rightarrow CH_4 + CO_2$	(4.8)	-33.5
• Steam reforming of acetone		
$CH_3COCH_3 + 5H_2O \rightarrow 3CO_2 + 8H_2$	(4.9)	246.1
• Steam reforming of methane		
$CH_4 + 2H_2O \rightarrow CO_2 + 4H_2$	(4.10)	165.1
$CH_4 + H_2O \rightarrow CO + 3H_2$	(4.11)	206.1
• Reverse water gas shift reaction		
$H_2 + CO_2 \rightarrow H_2O + CO$	(4.12)	41.1
• Water gas shift reaction		
$H_2O + CO \rightarrow H_2 + CO_2$	(4.13)	-41.1
• Methanation		
$CO + 3H_2 \rightarrow CH_4 + H_2O$	(4.14)	-206.1
$CO_2 + 4H_2 \rightarrow CH_4 + 2H_2O$	(4.15)	-165.1
• CO disproportionation (Boudouard reaction)		
$2CO \rightarrow C + CO_2$	(4.16)	-172.4
• Acetic acid decomposition		
$CH_3COOH \rightarrow C + CO_2 + 2H_2$	(4.17)	41.3
• Methane decomposition		
$CH_4 \rightarrow C + 2H_2$	(4.18)	74.8
• Acetone polymerization		
$CH_3COCH_3 \rightarrow$ Oligomerization $\rightarrow$ Carbon deposits	(4.19)	-
• Elimination of carbon deposition		
$C + H_2O \rightarrow CO + H_2$	(4.20)	131.3
$C + CO_2 \rightarrow 2CO$	(4.21)	172.4
$C + O_2 \rightarrow CO_2$	(4.22)	-393.5

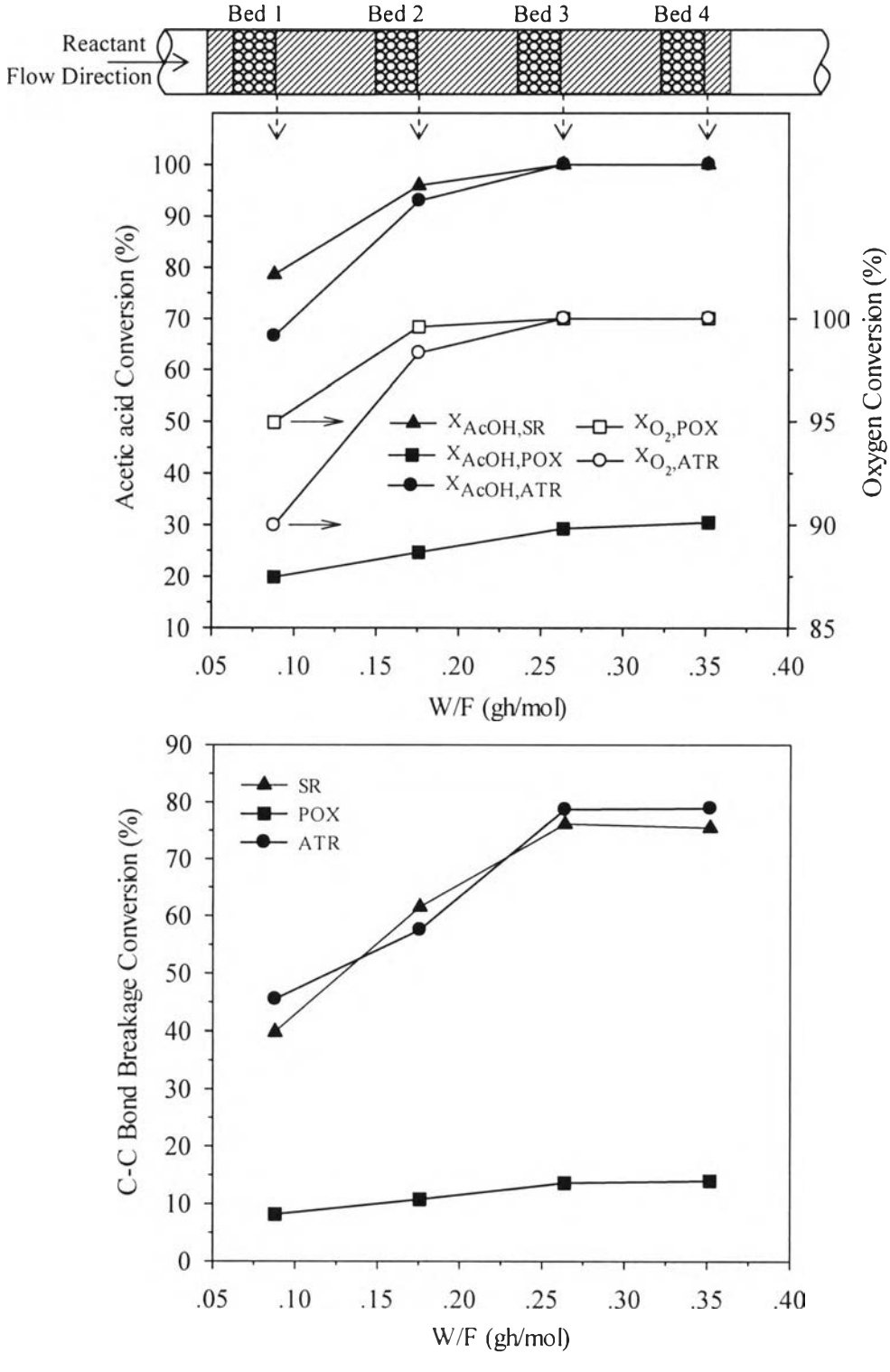

Figure 4.4 Conversion of reactants and C-C bond breakage conversion over 15%Ni/Ce75Zr25Ox catalyst in relation to contact times (W/F), S/C = 6 (for SR and ATR), O_2/Acetic acid = 0.35 (for POX and ATR), T = 650 °C, and total flow rate = 170 ml/min.

As shown in Figure 4.4, acetic acid conversion under SR conditions at 0.088 $g \cdot h \cdot mol^{-1}$ is ca. 80 % which is higher than that of ATR and POX about 10 % and 60 %, respectively. Then, acetic acid conversion is increased significantly with increasing contact time and completely consumed at 0.264 $g \cdot h \cdot mol^{-1}$ for both SR and ATR processes due to a longer contact time allowing a more occurrence of reaction steps between active sites of the catalyst surface and feed reactants. While a slight increase in acetic acid conversion and incomplete consumption was achieved only with POX due to the limitation of O_2 feeding. To compare the product distribution between ATR and POX processes, O_2 was fed at the same O_2/acetic acid molar ratio of 0.35. About 90 % and 95 % of O_2 conversion were observed after the reaction had proceeded at 0.088 $g \cdot h \cdot mol^{-1}$ under ATR and POX, respectively.

In this work the C-C bond breakage conversion is defined as the process performance of cracking acetic acid into CO, CO_2, and CH_4 as shown in Figure 4.4. ATR shows higher cracking activity than SR due to its higher CO_2 yield except for the 2nd catalyst bed (0.176 $g \cdot h \cdot mol^{-1}$) which would be discussed later. After the 3rd catalyst bed, C-C bond breakage conversion is reached the highest value of ca. 80 % under ATR conditions and could not be 100 % for all processes due to the coke or intermediate formations such as acetone. However, the lowest C-C bond breakage conversion in all observed regions was observed in POX. This could be enunciated that the process performance for acetic acid cracking was decreased in the following order: ATR>SR>POX. Typically, acetone polymerization (Equation 4.19) producing carbon deposited was more suppressed and acetic acid tended to crack into single-carbon containing products in ATR process resulting in less carbon formation when compared to SR and POX processes (An *et al.*, 2011; Hu *et al.*, 2013).

As demonstrated in Figure 4.5, there was a substantial increase in H_2 yield with increasing contact time over SR and ATR processes as compared to POX conditions. SR exhibits much higher activity for hydrogen production than POX due to its better activity for water gas shift reaction (Equation 4.13). However, H_2 production under ATR conditions appears ca. 10 % lower than SR conditions in all observed regions, after the 3rd catalyst bed (0.264 $g \cdot h \cdot mol^{-1}$), the H_2 production on both SR and ATR becomes closer to the thermodynamic equilibrium value at this temperature (650 °C) as reported by Vagia and Lemonidou (2008 and 2010).

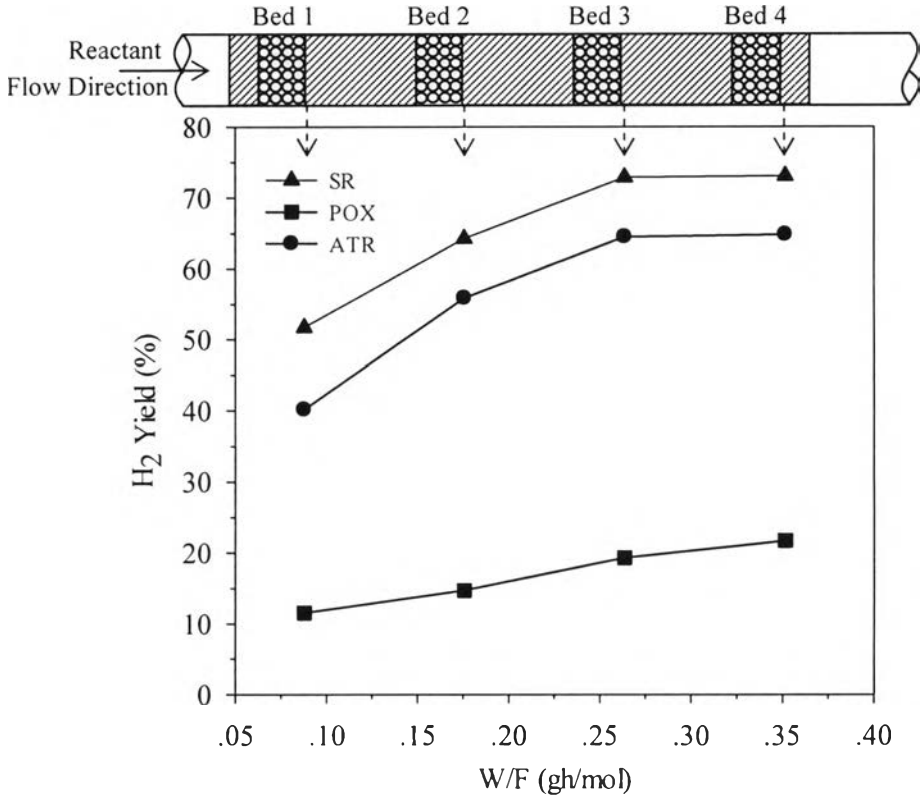

Figure 4.5 Hydrogen production over 15%Ni/Ce75Zr25Ox catalyst in relation to contact times (W/F), S/C = 6 (for SR and ATR), O_2/Acetic acid = 0.35 (for POX and ATR), T = 650 °C, and total flow rate = 170 ml/min.

As shown in Figure 4.6, CO_2 yield under SR appears to increase significantly in a monotonous mode, whereas under ATR conditions, oxidations of acetic acid (Equations 4.3-4.5) accompanied with ketonization reaction (Equation 4.6), acetic acid cracking (Equation 4.8), and WGS reaction (Equation 4.13) might occur resulting in the highest CO_2 production at the 1st catalyst bed (0.088 $g \cdot h \cdot mol^{-1}$). Due to the limitation of O_2 feeding and nearly complete consumption of O_2 after the 1st catalyst bed. CO_2 was slightly produced followed by WGS reaction (Equation 4.13) leading to higher CO_2 production again at the 3rd catalyst bed (0.264 $g \cdot h \cdot mol^{-1}$). However, it should be noticed that CO_2 selectivity under ATR exhibits the same trends as those of POX and SR at the front catalyst bed and the remainder of the catalyst beds, respectively.

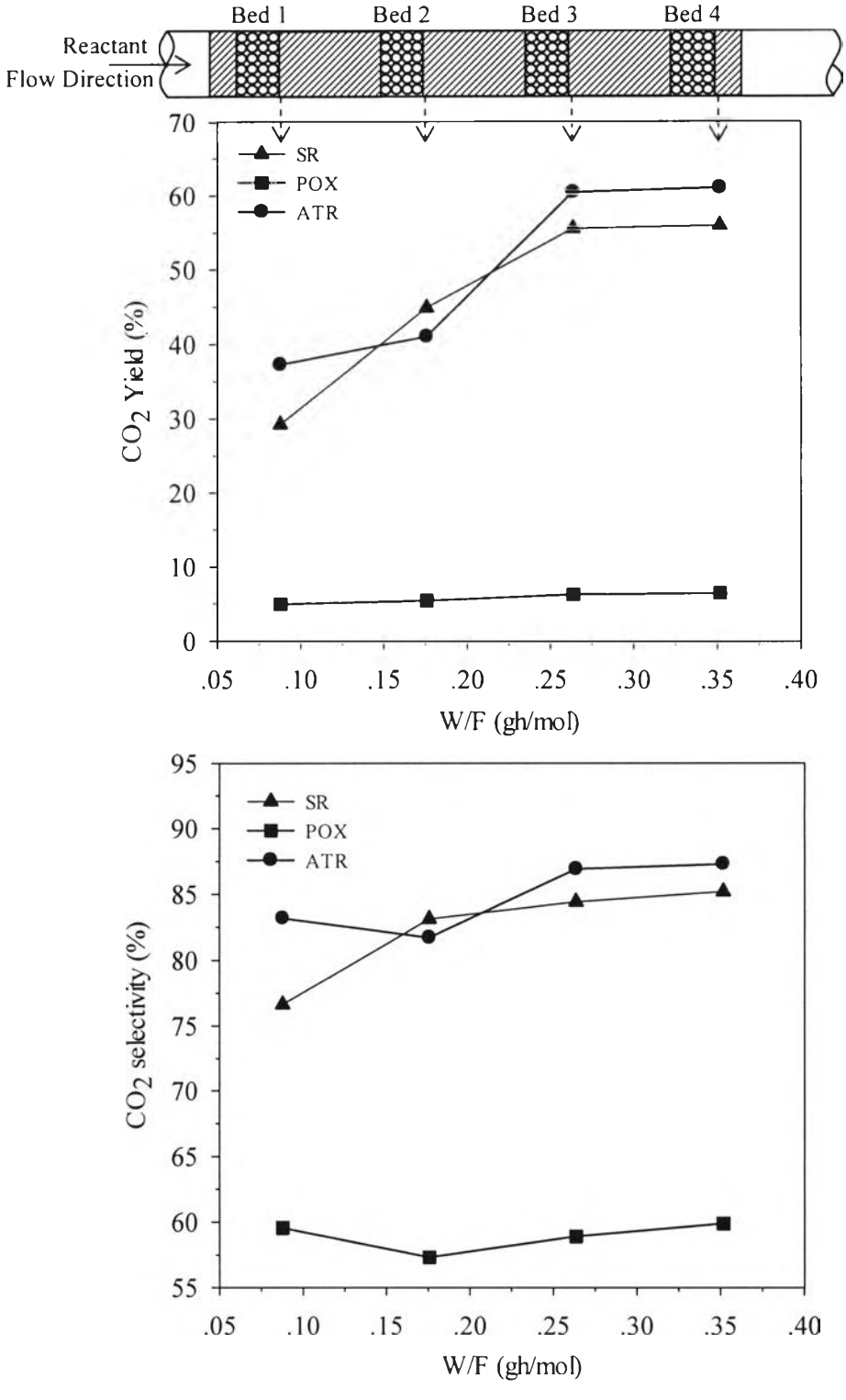

Figure 4.6 Carbon dioxide production and selectivity over 15%Ni/Ce75Zr25Ox catalyst in relation to contact times (W/F), S/C = 6 (for SR and ATR), O_2/Acetic acid = 0.35 (for POX and ATR), T = 650 °C, and total flow rate = 170 ml/min.

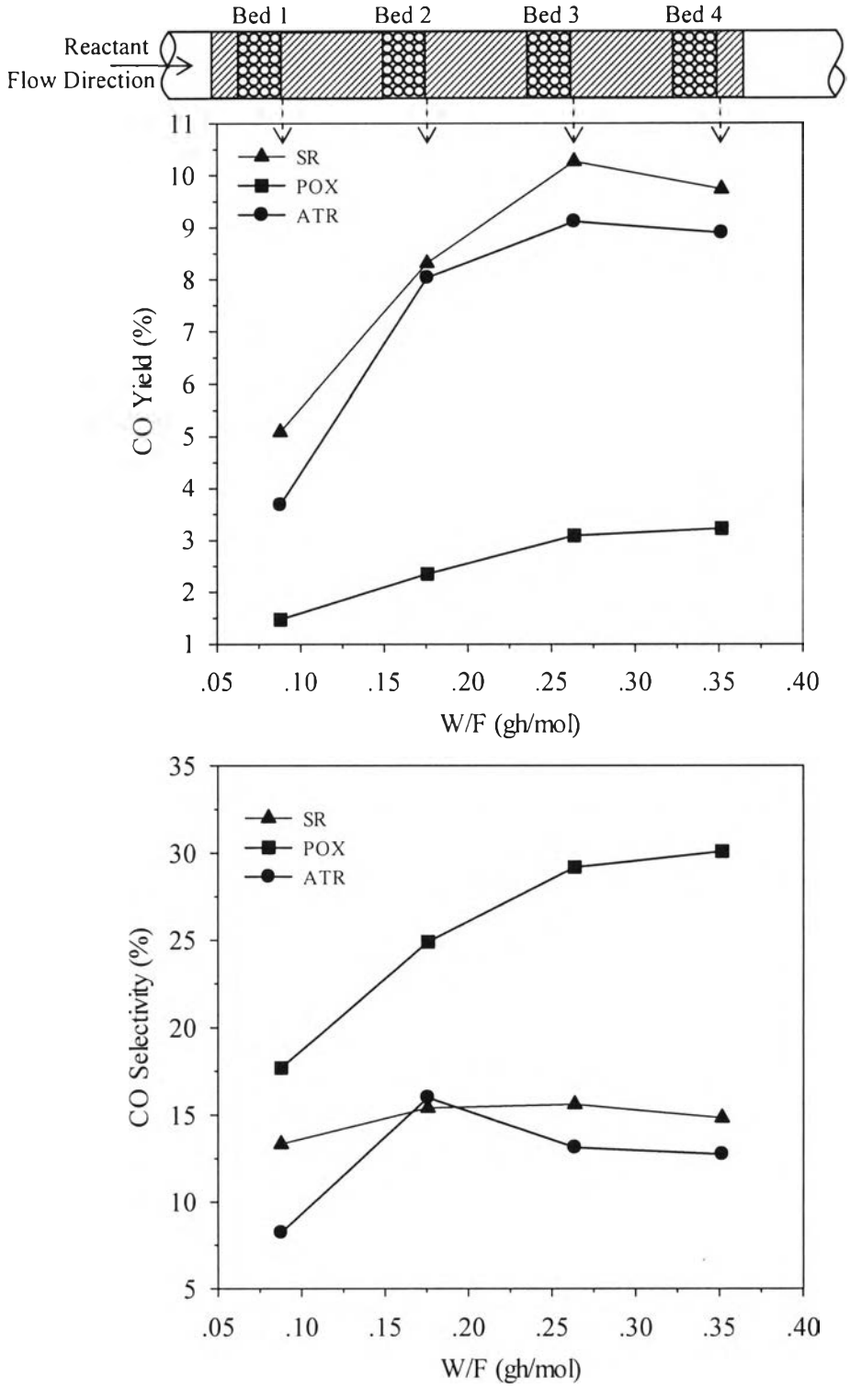

Figure 4.7 Carbon monoxide production and selectivity over 15%Ni/Ce75Zr25Ox catalyst in relation to contact times (W/F), S/C = 6 (for SR and ATR), O_2/Acetic acid = 0.35 (for POX and ATR), T = 650 °C, and total flow rate = 170 ml/min.

It can be seen from Figure 4.7 that all the processes produce a relatively small amount of CO (< 11 % yield) in which SR and ATR provide significant increases in CO yield up to the contact time of 0.264 $g \cdot h \cdot mol^{-1}$. However, the lowest CO content is produced by POX due to the lack of steam required for steam reforming to produce synthesis gas. For ATR process, it should be noted that both the CO and CO_2 selectivities behave similar to those of POX in a first half portion of the catalyst beds (0.088 to 0.176 $g \cdot h \cdot mol^{-1}$) and similar to those of SR in the remainder of the catalyst beds (above 0.176 $g \cdot h \cdot mol^{-1}$) suggesting that the different reactions occur along the catalyst bed under ATR conditions.

As shown in Figure 4.8, CH_4 yields for all the processes are infinitesimally detectable at the beginning (< 1 % yield). As an increase in the contact time, the complete consumption of CH_4 can be observed for SR and ATR processes due to the steam reforming of methane (Equations 4.10 and 4.11). However, a trace amount of CH_4 is increased continuously under POX as a function of contact time due to the lack of steam activation in the system and that CH_4 could not be reformed. Another undesired by-product, i.e., acetone generated from ketonization reaction (Equation 4.6) underwent further oligomerization reactions responsible for coke formation. As presented in Figure 4.9, a trace amount of acetone is produced at the catalyst bed inlet followed by decreased with increasing in contact time for all processes. Steam reforming of acetone (Equation 4.9) might be occurred under SR and ATR conditions leading to acetone consumption at the 3rd catalyst bed while the decreasing in POX might be due to the acetone polymerization (Equation 4.19) which could be predicted that huge amount of coke would be generated.

Previous work (Phongprueksathat, 2013) studied the decomposition of acetic acid or cracking reaction (Equation 4.7). It was found that acetic acid was still converted into H_2 and CO in the absence of other reactants at a specified temperature (650 °C) with high C-C bond breakage conversion around 50 %. Thus, based on the experimental results obtained in this work, it is postulated that under SR conditions at the 1st catalyst bed (0.088 $g \cdot h \cdot mol^{-1}$), the steam reforming of acetic acid (Equation 4.1) and decomposition of acetic acid (Equation 4.7) were the main routes for H_2 production while acetone and methane were produced from ketonization reaction (Equation 4.6) and decarboxylation of acetic acid (Equation 4.8), respectively. Then,

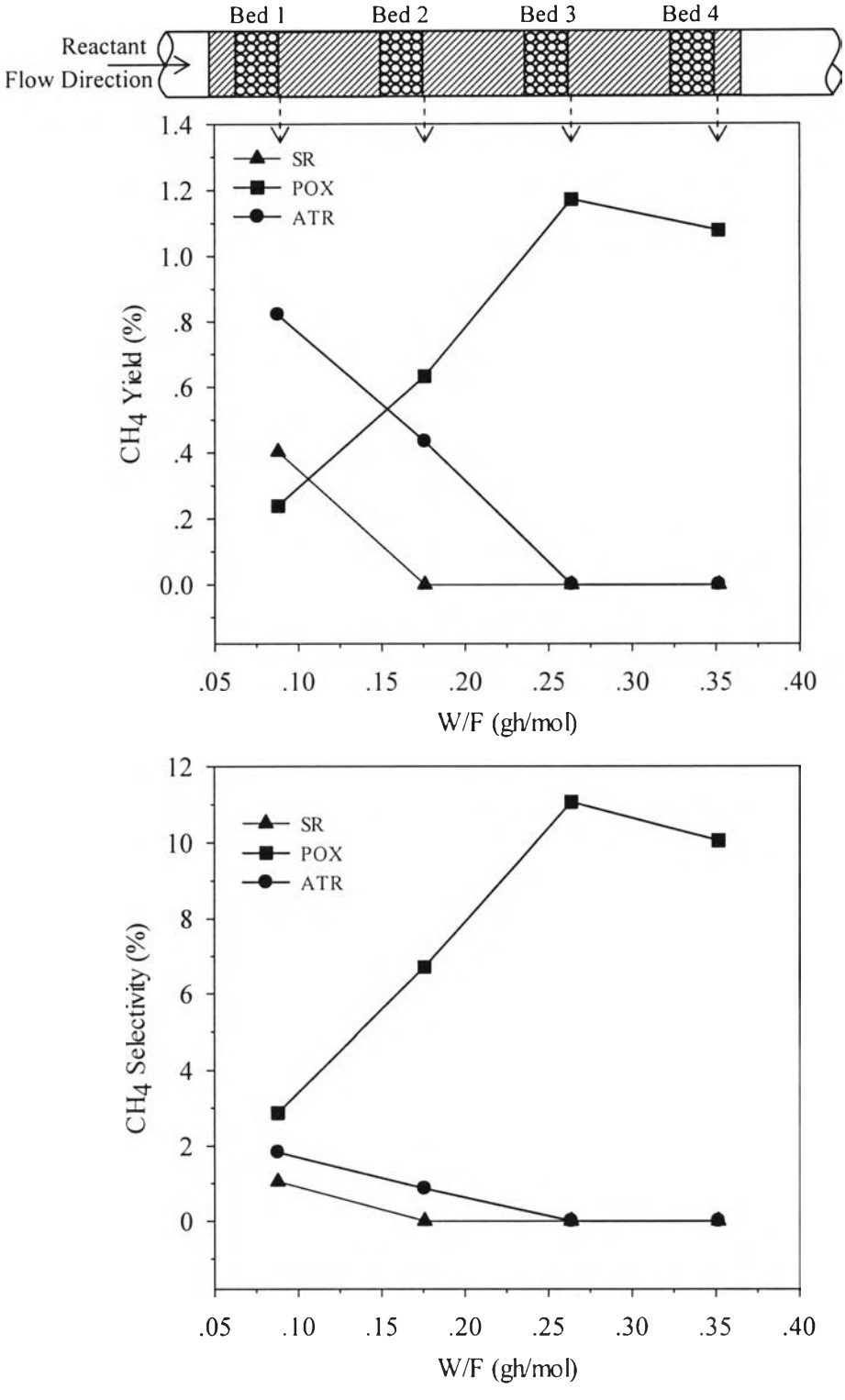

Figure 4.8 Methane production and selectivity over 15%Ni/Ce75Zr25Ox catalyst in relation to contact times (W/F), S/C = 6 (for SR and ATR), O_2/Acetic acid = 0.35 (for POX and ATR), T = 650 °C, and total flow rate = 170 ml/min.

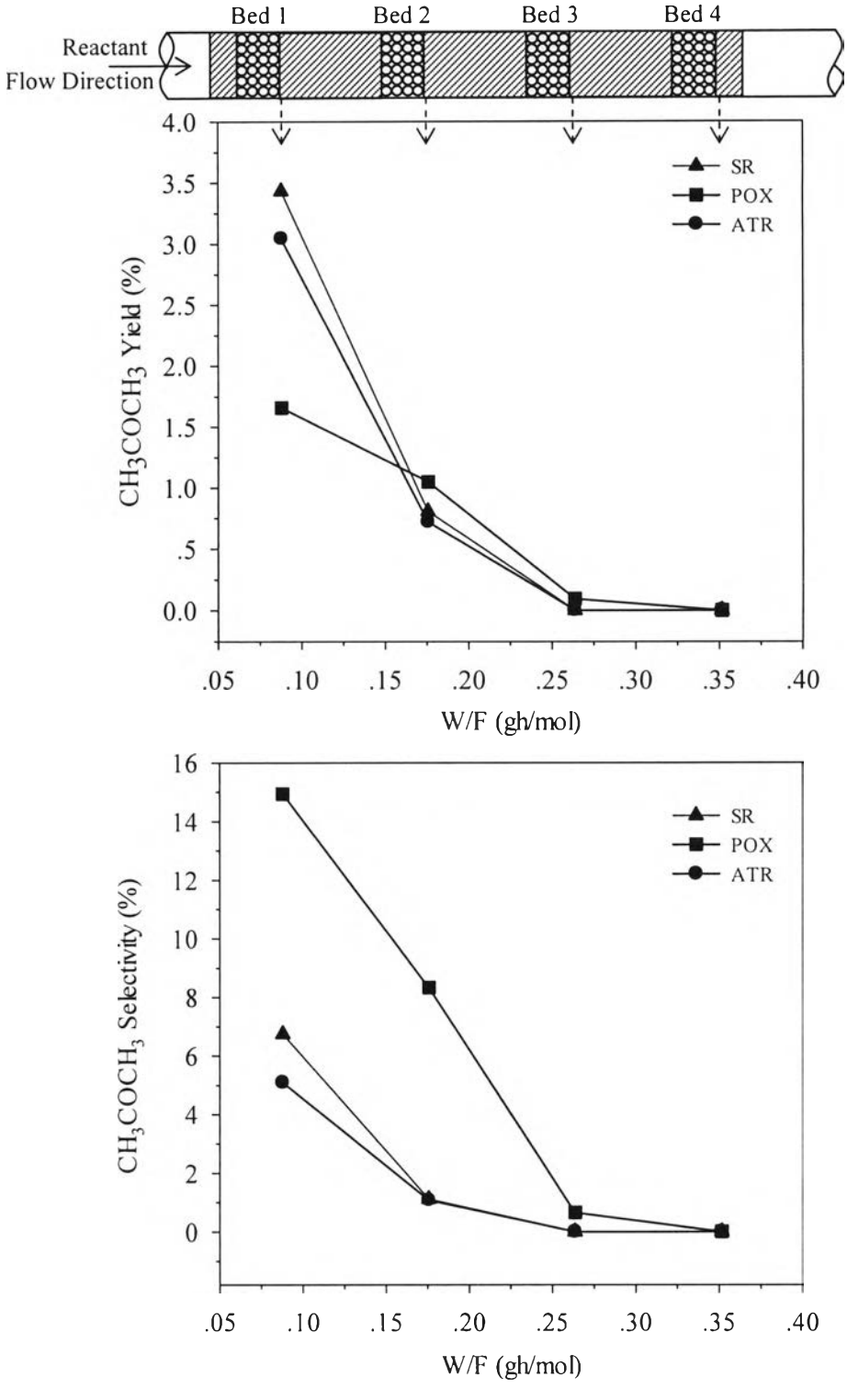

Figure 4.9 Acetone production and selectivity over 15%Ni/Ce75Zr25Ox catalyst in relation to contact times (W/F), S/C = 6 (for SR and ATR), O_2/Acetic acid = 0.35 (for POX and ATR), T = 650 °C, and total flow rate = 170 ml/min.

all steam reforming of acetic acid, acetone, and methane (Equations 4.1, 4.9, and 4.11, respectively) were taken place at the 2nd catalyst bed (0.176 $g \cdot h \cdot mol^{-1}$). At the 3rd catalyst bed (0.264 $g \cdot h \cdot mol^{-1}$), acetic acid and acetone were completely reformed allowing the water gas shift reaction to be the main reaction at the last catalyst bed (0.352 $g \cdot h \cdot mol^{-1}$) accordingly.

For POX, oxidation reactions of acetic acid (Equations 4.3-4.5) were the main routes for a first half catalyst beds with all available O_2 while the lowest in C-C bond breakage conversion and H_2 production were obtained due probably to the acetone polymerization (Equation 4.19) to carbonaceous compounds attached on the catalyst surface as to be mentioned in the next section. Moreover, CH_4 was still produced continuously as a function of contact time on which carbon deposited could be generated via methane decomposition (Equation 4.18).

Under ATR conditions, the reaction proceeds through two zones in series which are an exothermic oxidation zone followed by an endothermic steam reforming zone resulting in the earlier O_2 consumption over a short portion of the catalyst beds when compared to acetic acid conversion. Moreover, the high CO_2 yield attributed that exothermic reactions was the main reaction at the catalyst bed inlet. Whereas, the endothermic reaction was kinetically restricted at the higher gas velocities due to it much slower reaction rate. Then, the increased synthesis gas production accompanied with the decreased CO_2 yield (until 0.176 $g \cdot h \cdot mol^{-1}$) suggested that the reactions producing synthesis gas proceeded after the oxidation reactions were complete. These results are in agreement with those reported by several authors (Tomishige *et al.*, 2004; Simeone *et al.*, 2008b; Sato *et al.*, 2009).

A few research groups (Yamazaki *et al.*, 1996; Li *et al.*, 2004; Tomishige *et al.*, 2004) discovered that the type of catalytic metal would influence the mechanisms and reaction steps along the catalyst bed under ATR conditions. Of those, Tomishige *et al.* (2004) noticed that under O_2 atmosphere, metallic Ni (Ni^0) had a strong thermodynamic tendency to be converted into NiO (Ni^{2+}) by which the oxidized form of Ni is known to be an active for exothermic reactions, but not for endothermic reforming reactions. Based on the results on reactant conversion, it could be suggested that metallic Ni at the catalyst bed inlet was oxidized by O_2 to NiO under

ATR and POX conditions, which promoted the exothermic reaction followed by reforming reaction over reduced Ni in O_2-depleted zone down the length of the catalyst bed. This hypothesis was also verified by XPS analysis to investigate the oxidation states of the spent Ni catalysts after proceeding through SR, POX, and ATR processes. The Ni $2p_{3/2}$ XPS spectra of fresh, reduced, and each spent 15%Ni/Ce75Zr25Ox catalyst bed are depicted in Figure 4.10.

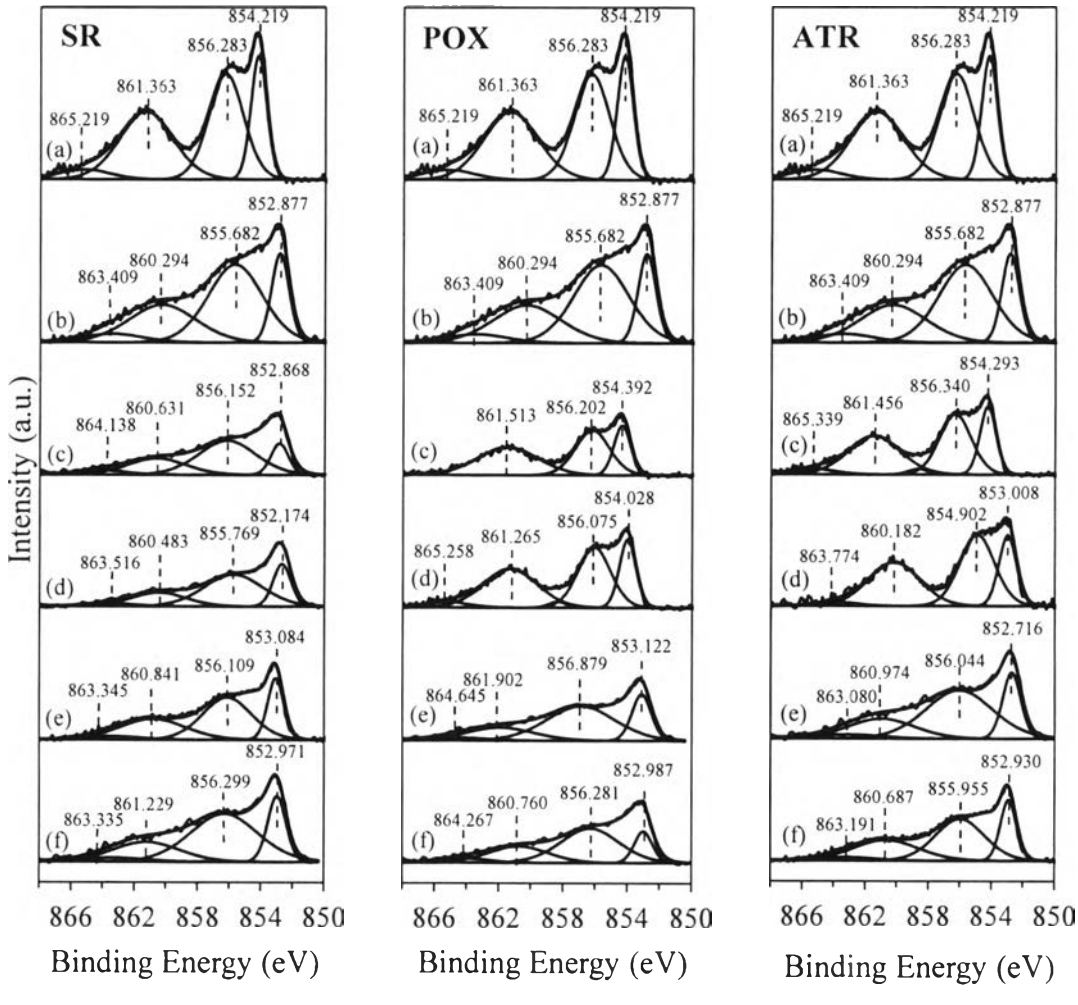

Figure 4.10 XPS spectra in Ni $2p_{3/2}$ region of (a) fresh 15%Ni/Ce75Zr25Ox catalyst, (b) reduced 15%Ni/Ce75Zr25Ox catalyst, (c) the 1st spent catalyst bed, (d) the 2nd spent catalyst bed, (e) the 3rd spent catalyst bed, and (f) the 4th spent catalyst bed over different processes (SR, POX, and ATR).

Prior to beginning the reactions, the catalyst was reduced according to the procedure mentioned in the experimental section. Hence, in the absence of O_2 as for SR spent catalysts, the XPS spectra of Ni $2p_{3/2}$ would be the same patterns as the reduced catalyst spectrum. On the contrary, in the presence of O_2 as for POX and ATR spent catalysts, their spectra would exhibit similar patterns to the fresh catalyst spectrum in the O_2-containing zone. The fresh 15%Ni/Ce75Zr25Ox catalyst (Figure 4.10 (a)) reveals two well resolved components at 854.22 and 856.28 eV and shake-up satellites at 861.36 and 865.22 eV. From the corresponding characteristic binding energy as shown in Table 4.4, the lowest binding energy component at 854.22 eV represent to the NiO species while a higher one at 856.28 eV has been attributed to Ni^{2+}-OH species or due to lattice distortions induced by the presence of Ni^{2+} vacancies (Solsona *et al.*, 2012). As compared to the values of the reduced 15%Ni/Ce75Zr25Ox catalyst (Figure 4.10 (b)), 852.88 and 855.68 eV and shake-up satellites at 860.29 and 863.41 eV are detected which binding energies are shifted by ca. 1 eV toward lower values when compared to those values from fresh catalyst attributed to the reduction of NiO into more Ni metallic form. Moreover, the ratio of relative area between the satellite peak at ca. 861 eV and the main Ni peak at ca. 854 eV is higher in fresh catalyst when compared to reduced catalyst as shown in Table 4.5. This satellite peak is very sensitive on the structure arrangement and the nature of Ni^{2+} surrounding atoms. Thus, the XPS results suggest a proportion of NiO detected in fresh catalyst higher than those achieved in reduced catalyst. As expected, the results of XPS for each spent catalyst bed were corresponding to the hypothesis proposed for which all of the spent catalyst beds under SR show the corresponding profiles with respect to the reduced catalyst due to the absence of O_2 in the system. For POX process, since O_2 was totally consumed after the 2^{nd} catalyst bed (as discussed above), the similar profiles to SR were obtained for the remainder of catalyst beds. In the case of feeding H_2O and O_2 simultaneously as for ATR, the similar results to POX were obtained for which the NiO form was the main type for the first two spent catalyst beds followed by the metallic Ni form for the remainder of catalyst beds.

Table 4.4 The chemical states of nickel with different electronic binding energies (Moulder *et al.*, 1992; Solsona *et al.*, 2012)

Electronic binding energy (eV)	Chemical state
852.6-852.9	Metallic Ni
853.4-854.4	NiO
855-856	Ni-OH
860-865	Shake-up Satellite

Table 4.5 Ratios of the satellite peak to the main Ni peak of fresh, reduced, and spent 15%Ni/Ce75Zr25Ox catalyst beds

Condition	Satellite area/Main Ni area					
	Fresh catalyst	Reduced catalyst	Bed 1	Bed 2	Bed 3	Bed 4
SR			1.733	0.993	1.390	1.107
POX	1.846	1.667	2.040	1.843	0.993	1.733
ATR			1.837	1.787	1.107	1.390

From the results discussed above it is indicated that the separate reaction zones existed under ATR conditions. Thus, the carbon deposited characteristics and amounts of carbon formation under different reaction conditions were further examined for a better understanding of the individual processes which will be discussed in the next section.

4.3 Characterization of Spent Catalysts

Carbon deposition is one of the major drawbacks and hard to be avoided in thermal processes causing the catalyst deactivation and loss of catalytic activity. The routes for carbon formation are quite complicated. CO disproportionation (Equation 4.16), acetic acid decomposition (Equation 4.17), methane decomposition (Equation

4.18), and acetone polymerization (Equation 4.19) all contribute to coke generation while H_2O, CO_2, and O_2 provide to the elimination of carbon deposition (Equations 4.20-4.22). Hence, the main aim of this section was to discuss the behaviors of the carbon deposited along the spent 15%Ni/Ce75Zr25Ox catalyst beds after progressed through SR, POX, and ATR of acetic acid. The qualitative and quantitative measurements of carbon deposited were performed by TPO technique. In order to confirm the results from TPO technique, TG-DTA technique was also carried out. XPS experiments were carried out to study the chemical states of the carbon species. In addition, TEM was employed to investigate the morphology of the carbon species.

Typically, TPO profiles of spent catalysts illustrate the exothermic peaks which are attributed to the combustion of coke deposition at different temperatures related with different coking mechanisms and properties. In all cases as shown in Figure 4.11, the peaks around 590 °C appear for each spent catalyst bed with the descending intensity from the 1st to 4th ones. However, another broad peak was also observed at ca. 500 °C close to the main peak in some cases indicative the different structure of filamentous carbon as will discussed in XPS C 1s and TEM results. For POX spent catalysts, Figure 4.11 (b) obviously illustrates the other peaks at ca. 270 °C with the same trend in intensity as that of high temperature peaks (~590 °C). Noticeably, such peaks are also observed with care for SR spent catalysts but relatively infinitesimal intensity (Figure 4.11 (a)). Figure 4.11 (c) presents a combination of TPO profiles for SR and POX spent catalysts in which, for ATR, the profiles for the first two spent catalyst beds are similar to those of POX whereas the ones for the remaining spent catalyst beds are similar to those of SR. This suggests that the different reactions take place along the catalyst beds under ATR process.

The results in the present work are in agreement with many researches (De Lima *et al.*, 2008; Vegia and Lemonidou, 2010; Wu and Liu, 2010; Li *et al.*, 2012b). They mentioned that graphitic or filamentous carbon was the main type of carbon deposited on the active sites of Ni catalyst, which burned around 600 °C. For the low-temperature peak (290 °C), indicated to the adsorbed amorphous carbonaceous or oligomers formed on the support as easily oxidized by steam. They also reported that these carbonaceous compounds could be considered as the precursor of coke by transformation to filamentous carbon.

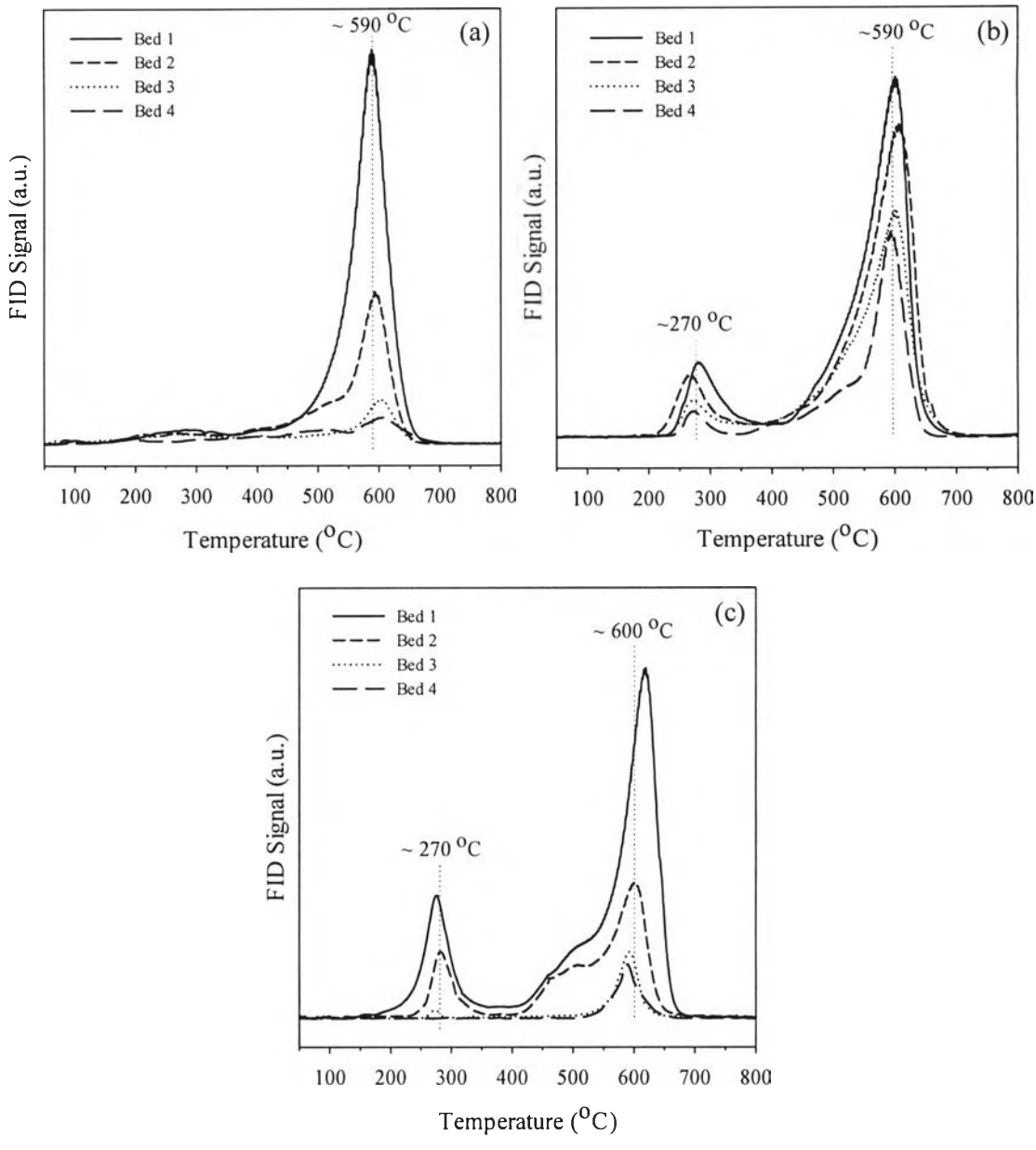

Figure 4.11 TPO profiles of each spent catalyst bed for (a) SR, (b) POX, and (c) ATR of acetic acid with a heating rate of 10 °C/min, an oxidizing gas containing 5 % O_2 in He with a flow rate of 20 ml/min.

The quantity of coke and coke profiles on individual beds of spent catalyst under different processes are summarized in Table 4.6 and Figure 4.12, respectively. As expected, the intensity from TPO profiles related to the amount of carbon formation. The first spent catalyst bed exhibits higher coke formation than the lower catalyst beds due to the incomplete conversion of acetic acid and the potential

precursors as CH_4 and acetone were produced at this catalyst bed leading to the favorable routes for coke formation (Equations 4.16-4.19). For the last catalyst bed, acetic acid was totally consumed and the precursors also reformed resulting in less coke detected in this bed, except for POX process which acetic acid and CH_4 still remained in high content. ATR exhibited a better activity with less carbon formation as compared to SR and POX might be due to the synergetic effect of H_2O and O_2. The addition of water favored the water gas shift (Equation 4.13) and suppression of carbon deposited (Equation 4.20) to produce H_2-rich gas production (Wu and Liu, 2010). Since an ease of reducibility and a good oxidation of the Ce75Zr25Ox mixed oxide could promote the oxidation of carbon precursors (Equation 4.22) on surface to gaseous carbon-containing as CO and CO_2, leading to the surface vacancy of active oxygen (O_s) which would be replaced by O_2 feeding into the system (Aneggi *et al.*, 2012; Thaicharoensutcharitthum *et al.*, 2011). For this reason, it could be concluded that the quantity of coke formed during those processes was decreased in the following order: POX>SR>ATR. For the results of TG-DTA analysis as shown in Table 4.6 and Figure 4.13, the derivative weight loss profiles exhibit similar to TPO technique which coke was burnt at ca. 550 °C under all processes and at ca. 250 °C only in POX and at the top portion of spent catalyst in ATR. However, another broad peak at ca. 500 °C could not detected by TG-DTA technique as same as TPO results due to the sensitivity of instruments. In addition, the quantity of coke and coke profiles from TG-DTA technique present the same trend as TPO results.

Table 4.6 Amounts of carbon formation on individual beds of spent catalyst after proceeded through SR, POX, and ATR of acetic acid

Catalyst Bed	Carbon Formation (wt%)					
	TPO			TG-DTA		
	SR	POX	ATR	SR	POX	ATR
1	9.59	39.77	4.79	10.01	48.61	5.05
2	5.98	38.85	2.51	8.22	47.40	3.20
3	1.99	35.20	0.89	2.37	43.80	1.41
4	1.06	31.83	0.60	1.13	43.75	0.57

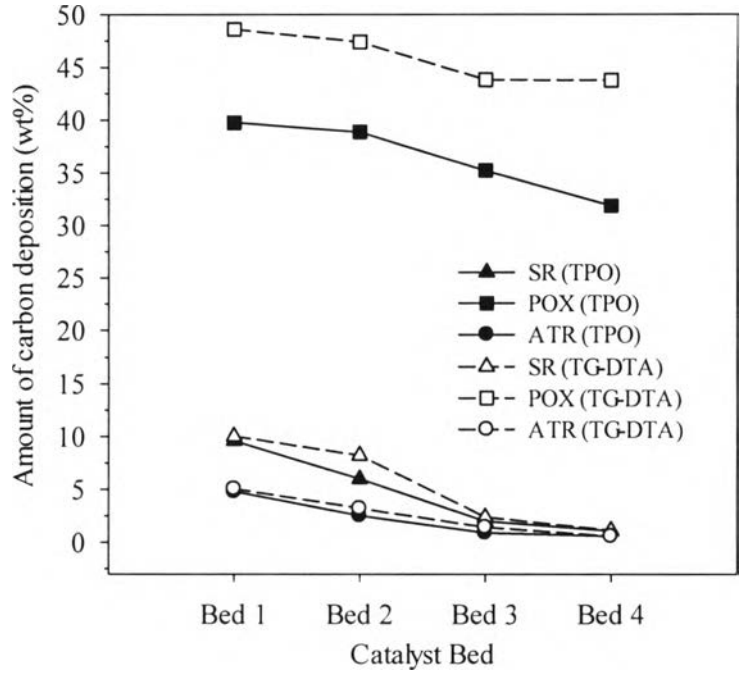

Figure 4.12 Coke profiles by TPO and TG-DTA techniques on individual beds of spent catalyst after proceeded through SR, POX, and ATR of acetic acid.

The XPS of C 1s spectra were scanned in order to examine the carbon species on the spent catalyst as depicted in Figure 4.14. Under SR conditions, the spectra are fitted with two peaks and their corresponding characteristic binding energy is summarized in Table 4.7. The strong peaks around 283-284 eV are related to a group of filamentous carbon which the different peaks are attributed to the different structure of filamentous carbon and burnt in the range of 500-600 °C as shown in TPO results. The weak peak at ca. 288 eV is attributed to adsorbed carbonaceous compounds or amorphous carbon which transformed from acetic acid to oligomer compound and attached on the catalyst surface. This peak corresponds to the TPO results which burnt at ca. 270 °C. It is well known that amorphous carbon is easier to be gasified by steam than filamentous carbon. For this reason, SR showed the higher performance in gasification of amorphous carbon as compared to POX by disappearance of amorphous peak in all of spent catalyst beds. As expected, the XPS of C 1s under ATR conditions exhibited the same behavior as POX at the first two spent catalyst beds followed by the similar profiles as SR down the rest of the catalyst beds.

Table 4.7 The chemical state of carbon with different electronic binding energy (Moulder *et al.*, 1992; An *et al.*, 2011)

Electronic binding energy (eV)	Chemical state
283-284	Graphitic carbon
285.2-286.2	-C-C
287.7-288.9	-C=O

In order to prove whether the peak at ca. 290 °C in both of TPO and TG-DTA were attributed to the oxidation of amorphous carbon, An *et al.* (2011) investigated by burned the spent Ni catalyst to 550 °C under air atmosphere followed by XPS analysis. They found only filamentous carbon peak was detected by XPS. This indicated that the carbon species removed below 550 °C was amorphous carbon and the remaining was almost filamentous carbon which oxidized around 600 °C as shown in TPO and TG-DTA results. Moreover, they also studied the conversion of the carbon species from CH_4 decomposition over Ni catalyst. The result revealed that amorphous carbon could be transformed into more filamentous carbon if amorphous carbon was not gasified by water or other oxides. Based on the results, the disappearance of amorphous carbon under SR condition was caused by the gasification or transformation to filamentous carbon.

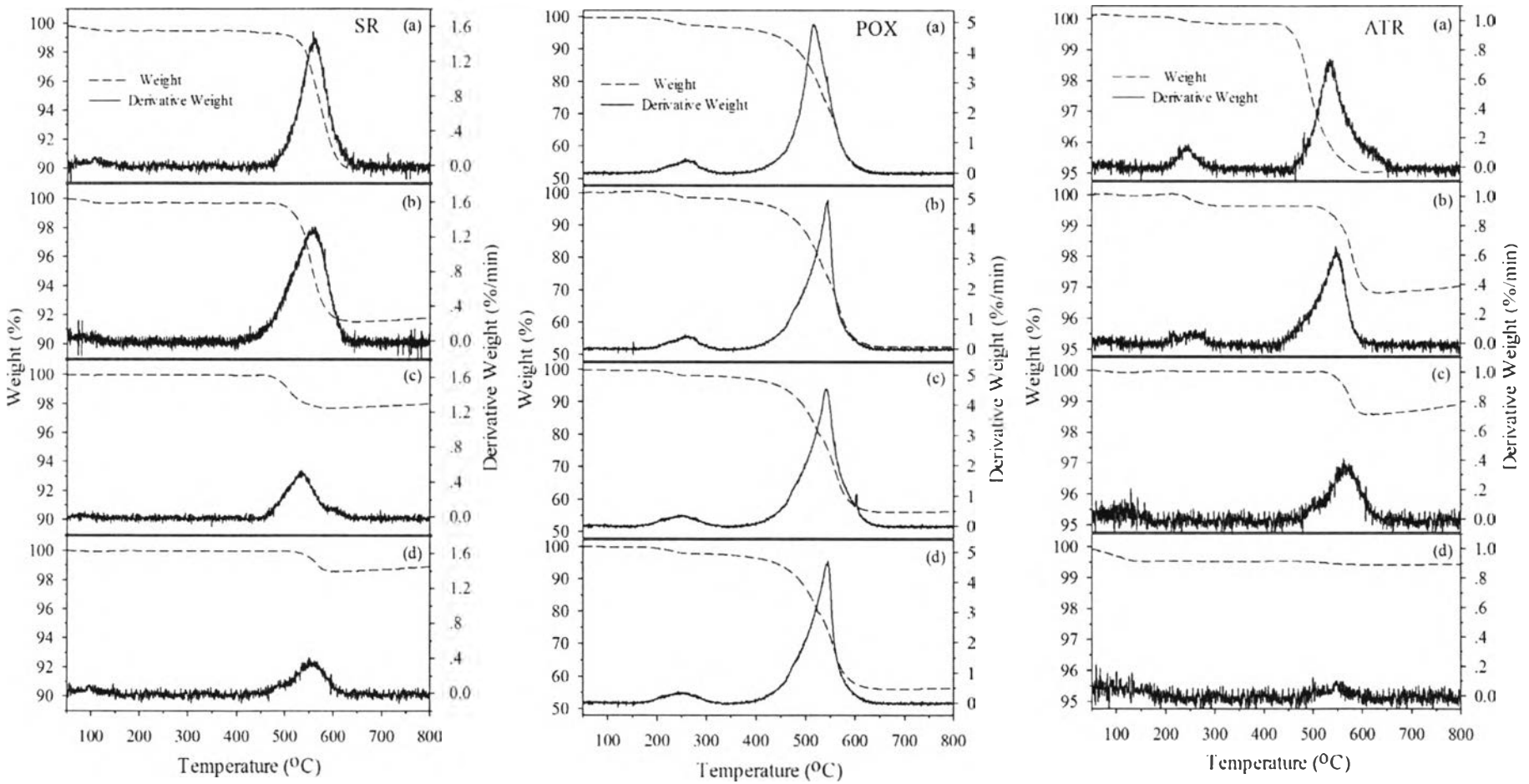

Figure 4.13 TG-DTA profiles of the spent catalyst under different processes (SR, POX, and ATR) with heating rate of 10 °C/min, an oxidizing gas containing O_2 in N_2 with a flow rate of 20 ml/min; (a) the 1st bed, (b) the 2nd bed, (c) the 3rd bed, and (d) the 4th bed.

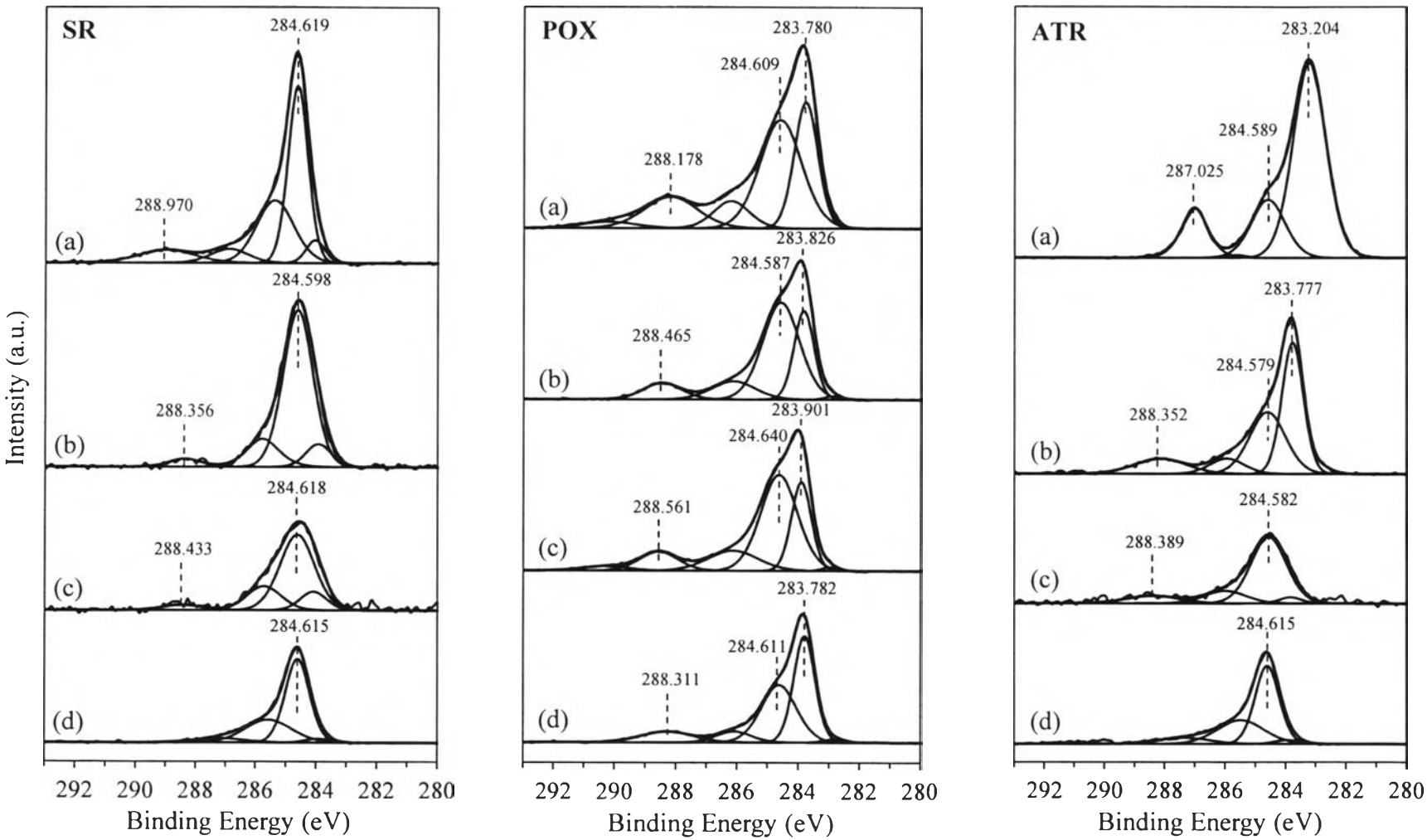

Figure 4.14 XPS spectra in C 1s region of spent catalyst beds; (a) the 1st bed, (b) the 2nd bed, (c) the 3rd bed, and (d) the 4th bed.

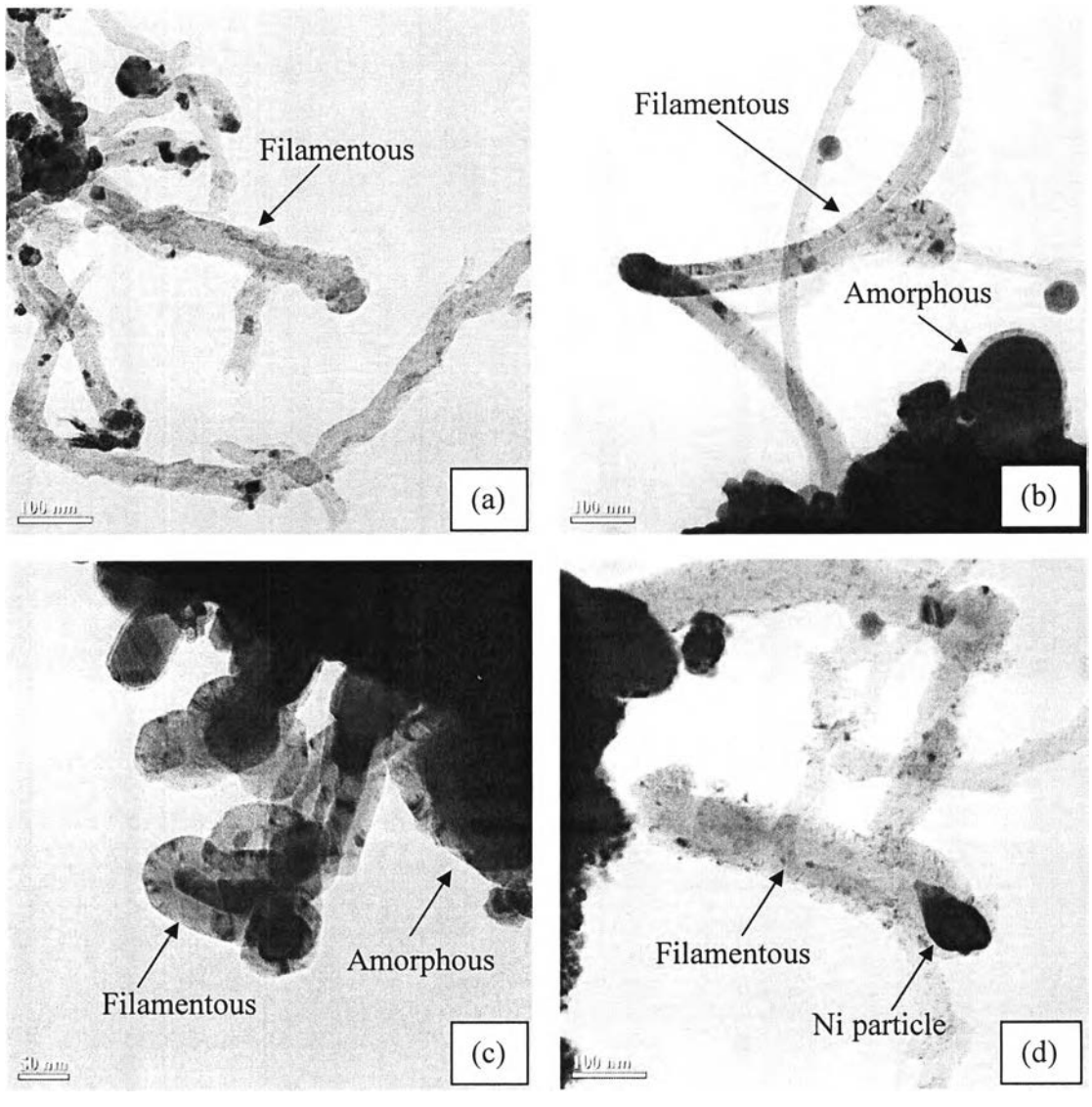

Figure 4.15 TEM images of the spent catalysts after activity tests of (a) SR-the 1st bed, (b) POX-the 1st bed, (c) ATR-the 1st bed, and (d) ATR-the 3rd bed.

TEM images proved that carbon species deposited over different processes had different structure as shown in Figure 4.15. The first spent catalyst bed after running SR process (Figure 4.15 (a)) was found to be covered with a lot of filamentous carbon. The filamentous carbon had a hollow nanotube structure with average diameter around 30 nm. It was also observed that a lot of Ni metal particles are incorporated at the tips of the carbon nanotubes. According to Takanabe *et al.* (2004) and Wu and Liu (2010), they suggested that this type of carbon was unique to

Ni because the carbon atoms were soluble in the metal lattice and its nucleation into grapheme layers at the metal-support interface. Then the Ni particle was forced to break away from the catalyst main body. Finally, a carbon nanotube formed. In contrast, less tubular carbon species with much thicker (~45 nm) were observed over the catalyst bed inlet for POX (Figure 4.15 (b)). Moreover, a heavy carbon coating was formed on the support, which related to the amorphous carbon or carbonaceous compounds as mentioned in the TPO, TG-DTA, and XPS results. Because there was no water feeding in POX process, the limitation of carbon elimination was tiny leading to large amount of carbon formation. The similar carbon formation behaviors to POX and SR were obtained by the first and the third spent catalyst beds for ATR, respectively (Figures 4.15 (c) and 4.15 (d)).

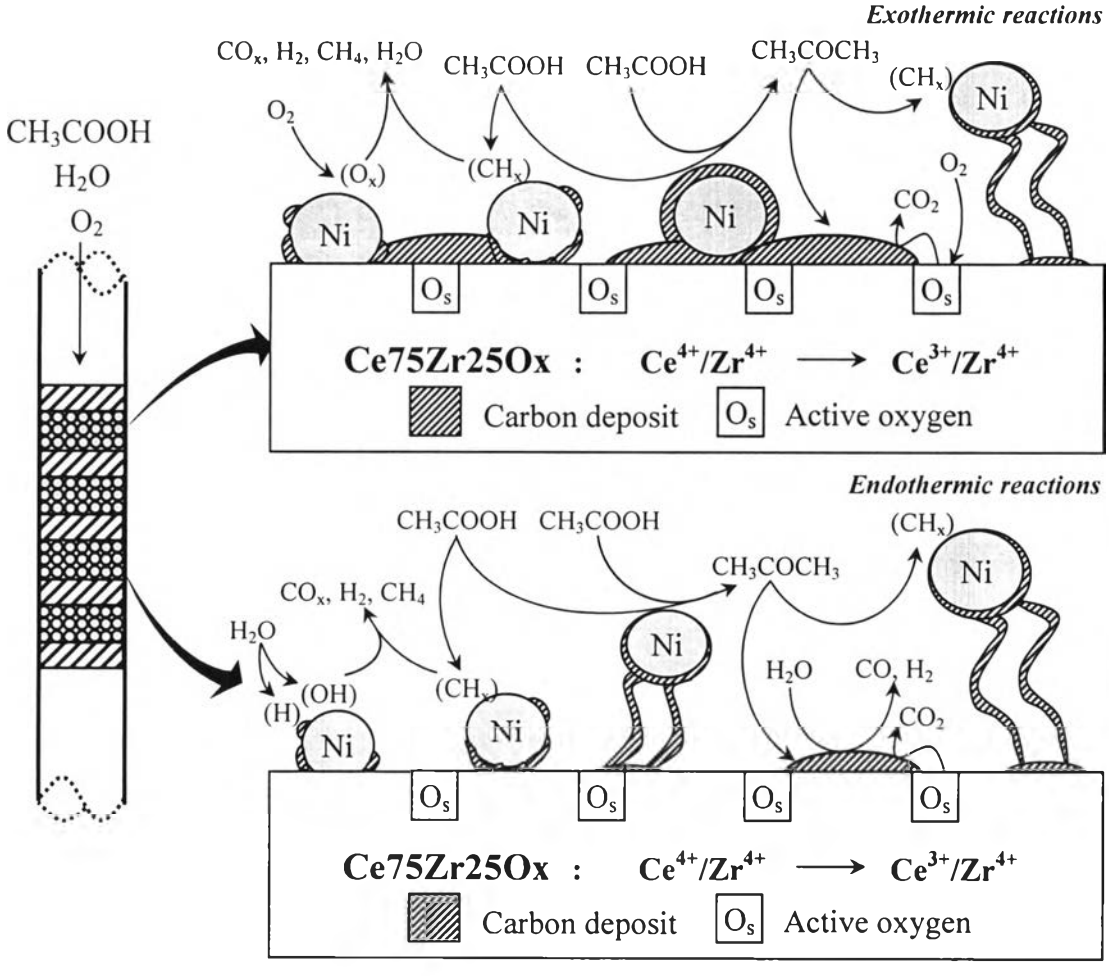

Figure 4.16 The proposed mechanism diagrams of the reaction pathways for ATR of acetic acid and coke formation on 15%Ni/Ce75Zr25Ox catalyst.

The results obtained in this part revealed the facts that the carbon deposition states on catalyst surface were significantly different due to the different reaction conditions. From the catalytic activity results accompanied with coke characterization results as discussed above, the proposed mechanism diagram of the reaction pathways for ATR of acetic acid and coke formation on 15%Ni/Ce75Zr25Ox catalyst are summarized in Figure 4.16.